Two-step hierarchical micromechanics model of partially saturated porous composites doped with ellipsoidal particles with interface effects

Enrique García-Macías[a,*], Rafael Castro-Triguero[c], Filippo Ubertini[b]

[a]*Department of Continuum Mechanics and Structural Analysis, School of Engineering, Universidad de Sevilla , Camino de los Descubrimientos s/n, E-41092-Seville, Spain*
[b]*Department of Civil and Environmental Engineering, University of Perugia, Via G Duranti 93, Perugia 06125, Italy*
[c]*Department of Mechanics, University of Cordoba, Campus de Rabanales, Cordoba, CP 14071, Spain*

Highlights

- A consistent homogenization model is proposed for particle-loaded porous composites
- Soft and hard particle interphases are considered
- The effect of partially saturated pores is investigated
- Different geometries of voids are studied

Abstract

Recent advances in the manufacture of micro- and nano-composites have made it possible to produce new multifunctional materials. However, the development of theoretical models that assist their design still remains an open research issue. This paper presents a two-step hierarchical micromechanics approach for the mechanical homogenization of particle-reinforced porous composites, including particle/matrix interfacial bonding and porosity saturation effects. Firstly, the particle-reinforced matrix is homogenized by means of a double-inclusion approach. The interfacial bonding effect is accounted for by both compliant and hard interphases surrounding the particles. Secondly, another homogenization step is conducted by considering the particle-reinforced composite as a homogeneous matrix and voids as embedded inclusions. Pores saturation is also taken into account by means of homogeneous equivalent pores. Comparative analyses against experimental data are presented to demonstrate the effectiveness of the present approach, followed by detailed parametric analyses to illustrate the influence of the major micromechanical variables, including interphase thickness and stiffness, filler aspect ratio, porosity and saturation degree.

Keywords: Double-inclusion, Eshelby's tensor, Homogenization, Interphase, Porous composite

1. Introduction

Recent advances in the manufacture of micro- and nano-composites have made great strides forward in the development of new multifunctional materials with a broad spectrum of applications in many fields such as building engineering, aerospace, automotive, construction, or industry. There is no shortage of research works that report on innovative composite materials with high-performance properties such as metals [1], ceramics [2], strain sensing bricks [3], phase changing materials [4], polymers [5], or cementitious composites [6]. In particular, the increasing demand for lightweight structures with superior mechanical properties has promoted an increasing attention on porous composites. Examples such as composite ceramics, foam-like materials, or spray deposits, not only exhibit excellent mechanical properties, but also multifunctional capabilities including low thermal conductivity, piezoresistive properties, low apparent density, and low moisture absorption [7–9]. In this context, the development of accurate homogenization schemes to assist the design is of pivotal importance. Despite great efforts have been put into the modeling of micro- and nano-composites, features such as the interfacial bonding condition between constituent phases, as well as complex microstructures with unsaturated porosity, still remain open research issues.

*Corresponding author.
Email address: egarcia28@us.es (Enrique García-Macías)

Extensive experimental and numerical results have revealed the importance of interfacial bonding between phases in the mechanical and transport properties of composites [10–12]. In fact, there exist interphases with finite volume between the inclusions and the matrix which govern the load transfer capabilities of composites [13, 14]. Interphases are typically categorized into hard (non-overlapping) and soft (overlapping) interphases [15–17]. Hard interphases are those that possess higher stiffness values than the matrix and can be deemed as impenetrable coatings surrounding the particles. This is for instance the case of poly(butylene terephthalate) doped with organically-modified montmorillonite, where the experimental results by Chang *et al*. [18] and the recent numerical analyses of Zare and Rhee [19] revealed the existence of hard interphases with elastic modulus around sixteen times that of the pristine polymer. On the other hand, soft interphases are those that exhibit less stiffness than the matrix material and can be regarded as penetrable interphases. Such soft interfaces typically stem from microstructural defects or relatively high porosity at particle/matrix interfaces. A good example of compliant interphases can be the so-called Interfacial Transition Zones (ITZs) in cementitious materials [20, 21].

Considerable effort has been put into the study of the interface effects and diverse approaches have been proposed in the literature. Among them, it is worth noting the so-called spring-type interface models [22, 23]. These approaches consider both compliant or stiff coatings with zero volume, in such a way that the contact condition is satisfied by imposing the continuity of displacements and tractions across the particle/matrix interface. A second group of models are the so-termed functionally graded interface models [24, 25], which assume that the properties of the interface region smoothly vary along the radial direction of the particles. Finally, the last group of approaches are the interphase or core-shell models [17, 26, 27], which define interface regions as coating phases with finite volumes between the inclusions and the matrix. Along these lines, particle-reinforced composites can be viewed as three-phase composites, and diverse approaches can be found in the literature on the estimation of their overall elastic moduli. It is worth noting the Generalized Self-Consistent Method (GSCM) three-phase sphere model [28–30], in which the reinforcing particles are encapsulated in the interphases, and then in the matrix phase. Majewski *et al*. [31] investigated the effects of particle packing and size on the overall elastic properties of particulate random composites with hard interphases. To that aim, those authors used numerical periodic unit cells of crystal-type arrangements and random distribution of particles, as well as the GSCM method. Xu *et al*. [17] proposed a Mori-Tanaka approach in combination with an interphase model to account for both hard and soft interfaces. Those authors provided extensive sensitivity analyses to investigate the effect of interfacial characteristics on the overall elastic moduli of different nano- and micro-sized particle-reinforced composites. Other different approaches on the homogenization of three-phase composites can be also found in the literature, including Hashin and Shtrikman bounds models [32, 33], Differential Effective Medium (DEM) approximations [34], and other effective medium methods [35, 36].

Along with the interfacial properties in particle-reinforced composites, the presence of pores and voids within porous matrix materials also holds a considerable influence on the macroscopic elastic moduli. In particular, numerous works have reported about the porosity effects on the mechanical properties of cement-based materials [37, 38]. Also, some authors have applied mean-field homogenization methods to simulate the effect of porosity on the overall stiffness of porous composites. A noteworthy contribution was done by Guéguen *et al*. [39] who utilized the DEM model to predict the elastic properties of porous media. Miled *et al*. [40] investigated the elastic properties of porous expanded polystyrene concrete with mean-field homogenization methods, including the Mori-Tanaka, GSCM and DEM models. Poh *et al*. [41] presented a multi-step micromechanics approach to estimate the effective properties of porous ceramics doped with Carbon Nanotubes (CNTs). According to that model, the porous ceramic matrix is first homogenized using a classical Mori-Tanaka model and considering the ceramic material and voids as matrix and inclusion phases, respectively. In a second step, the overall constitutive properties are computed by the Mori-Tanaka model, considering the porous ceramic as a homogeneous matrix phase and CNTs as reinforcing fillers. Recently, Rahmouni *et al*. [42] proposed a homogenization technique based on the Mori-Tanaka model to investigate the influence of the degree of water saturation on the elastic and acoustic properties of calcarenite.

In light of the foregoing literature review, there is no comprehensive micromechanics framework for the analysis of partially saturated porous media loaded with nano- and micro-fillers with interface effects. The present work is thus aimed at devising a theoretical approach in order to address this lacuna. In particular, a two-step hierarchical micromechanics approach is proposed. In a first step, the matrix material doped with anisotropic monodisperse particles is homogenized by means of a double-inclusion approach. An interphase model is adopted to incorporate both compliant and hard particle/matrix interface characteristics. Following the works of Xu and co-authors [17, 43], the volume fractions of the interphases are explicitly defined by a constant thickness surrounding the particles. Furthermore, unsaturated voids are converted into equivalent homogeneous pores by means of a Reuss approximation. Afterward, the second step consists of the application of the Mori-Tanaka model to compute the macroscopic properties, considering the particle/matrix composites as homogeneous matrix phases and pores as embedded ellipsoidal inclusions. Comparison analyses against experimental data, along with detailed

parametric studies, are presented in order to demonstrate the validity and effectiveness of the present approach to accurately predict the overall properties of micro- and nano-sized particle-reinforced porous composites with interface effects.

This paper is structured as follows. Section 2 outlines the theoretical background of the proposed approach, including the analysis of particle-reinforced composites with interface effects in Section 2.1, and the homogenization of partially saturated voids into equivalent homogeneous pores in Section 2.2. Section 3 presents the numerical results and discussion and, eventually, Section 4 concludes this work.

2. Theoretical formulation

The proposed two-step hierarchical homogenization model is schematically presented in Fig. 1. Firstly, Step I.A consists of a double-inclusion approach comprising the matrix material, particles, and interphases. Furthermore, the effect of partially saturated voids is accounted for by means of equivalent homogeneous pores (Step I.B in Fig. 1). Afterward, the overall elastic moduli of the composite are computed in Step II. In this case, the previously homogenized properties are drawn into a two-phase Mori-Tanaka homogenization approach, where matrix and inclusion phases are assumed to be the homogenized particle-reinforced matrix and equivalent pores, respectively. Throughout the text, a boldface letter stands for a fourth-order tensor, $\mathbf{A} \equiv A_{ijkl}$, while $\mathbf{I}$ denotes the fourth-order identity tensor, and a colon between two tensors represents the inner product, $\mathbf{A} : \mathbf{B} \equiv A_{ijkl}B_{klmn}$.

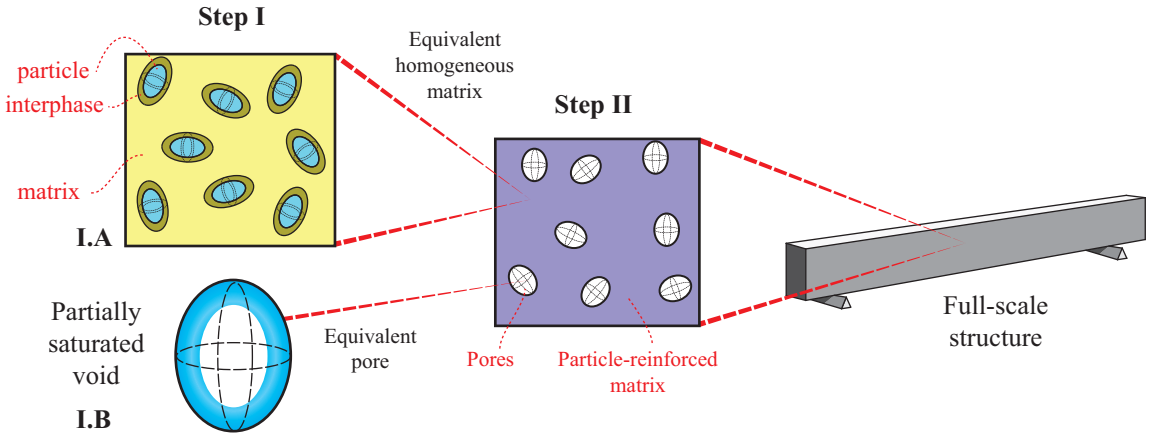

Figure 1: Schematic representation of the proposed two-step micromechanics model.

2.1. Step I.A: Particle-reinforced composites with interface properties

Let us define a three-phase particle-reinforced composite consisting of a hosting matrix Ω_m, an ellipsoidal inclusion Ω_p, and a surrounding interphase Ω_i as shown in Fig. 2 (a). In accordance with the notation of Hori and Nemat-Nasser [44], regions Ω_p and Ω_i define a double inclusion denoted by $R = \Omega_p \cup \Omega_i$. It is assumed that Ω_p, Ω_i and Ω_m are uniform media with elastic tensors $\mathbf{C}_p$, $\mathbf{C}_i$ and $\mathbf{C}_m$. Hence, the stress tensor $\boldsymbol{\sigma}(x)$ at a material point x can be related to the corresponding strain tensor $\boldsymbol{\varepsilon}(x)$ as:

$$\boldsymbol{\sigma}(x) = \begin{cases} \mathbf{C}_p : \boldsymbol{\varepsilon}(x), & \forall x \in \Omega_p \\ \mathbf{C}_i : \boldsymbol{\varepsilon}(x), & \forall x \in \Omega_i \\ \mathbf{C}_m : \boldsymbol{\varepsilon}(x), & \forall x \in \Omega_m \end{cases} \tag{1}$$

Let V denote the Representative Volume Element (RVE) of a linear elastic matrix doped with dispersed inclusions of Fig. 2 (b). It is assumed that the RVE contains a sufficient number of fillers in such a way that the overall properties of the composite are statistically represented [45]. The RVE is subjected to a far-field strain tensor $\boldsymbol{\varepsilon}^{\mathrm{o}}$ as shown in Fig. 2. The overall effective elasticity stiffness $\overline{\mathbf{C}}$ of the composite is defined by:

$$\overline{\boldsymbol{\sigma}} = \overline{\mathbf{C}} : \overline{\boldsymbol{\varepsilon}} \tag{2}$$

Throughout this work, the superscripts "p", "i" and "m" refer the corresponding quantity to the particle, interphase and matrix occupied portions of V. With this convention, the relationships between the total average strain and stress tensors in the RVE, $\overline{\boldsymbol{\varepsilon}}$ and $\overline{\boldsymbol{\sigma}}$, respectively, are defined by the rule of mixtures as follows:

$$\overline{\boldsymbol{\varepsilon}} = f_p \left\langle \overline{\boldsymbol{\varepsilon}}_p \right\rangle + f_i \left\langle \overline{\boldsymbol{\varepsilon}}_i \right\rangle + f_m \overline{\boldsymbol{\varepsilon}}_m = \boldsymbol{\varepsilon}^{\mathrm{o}} \tag{3}$$

$$\overline{\boldsymbol{\sigma}} = f_p \left\langle \overline{\boldsymbol{\sigma}}_p \right\rangle + f_i \left\langle \overline{\boldsymbol{\sigma}}_i \right\rangle + f_m \overline{\boldsymbol{\sigma}}_m = \boldsymbol{\sigma}^{\mathrm{o}} \tag{4}$$

where f_p, f_i and f_m stand for the volume fraction occupied by the particles, interphases and hosting matrix, and angle brackets $\langle \cdot \rangle$ represent volume average.

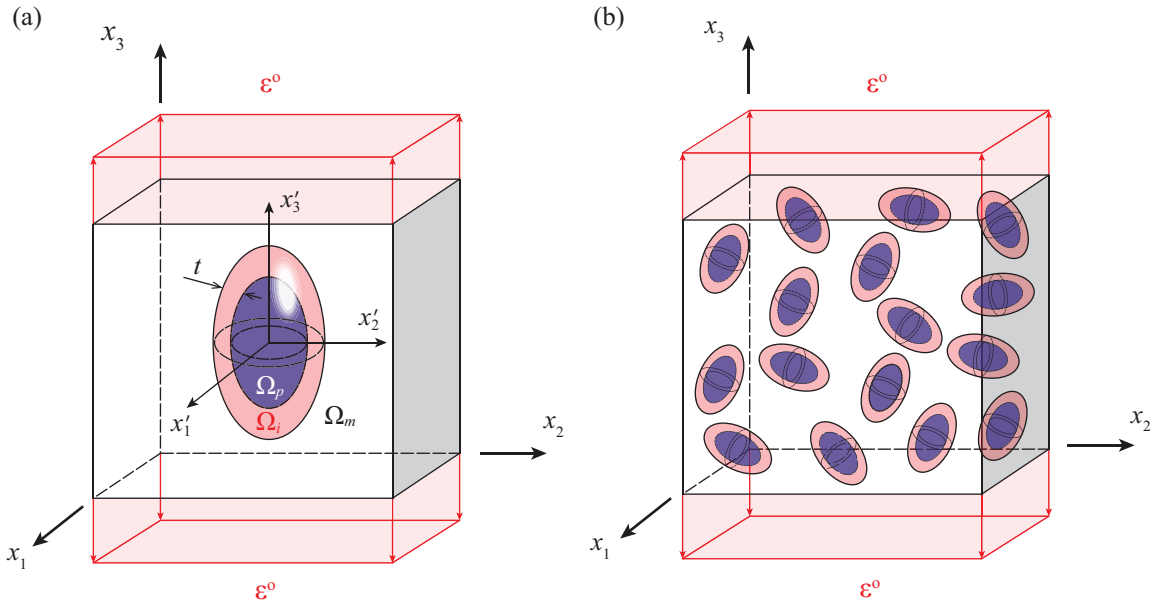

Figure 2: Schematic view for the predictions of the three-phase model using the coupling of Eshelby's equivalent inclusion theory (a) and Mori-Tanaka scheme (b).

To illustrate the application of the double inclusion model, the following eigenstrain is prescribed in R:

$$\boldsymbol{\varepsilon}^* = \begin{cases} \boldsymbol{\varepsilon}^*(x), & \forall x \in R \\ 0, & \forall x \notin R \end{cases} \tag{5}$$

Eigenstrains $\boldsymbol{\varepsilon}^*(x)$ produce perturbation strains $\boldsymbol{\varepsilon}^d(x)$ which are given by:

$$\boldsymbol{\varepsilon}^d_{ij}(x) = -\frac{1}{2} \int_R C_{klmn} \left[G_{ik,lj}(x-y) + G_{jk,li}(x-y) \right] \boldsymbol{\varepsilon}^*_{mn}(x) \mathrm{d}V_y = \int_R \Gamma_{ijmn} \boldsymbol{\varepsilon}^*_{mn}(x) \mathrm{d}V_y \tag{6}$$

where $\mathbf{G}(x-y)$ denotes the Green's function for an elastic solid, and a comma in the subscript denotes partial differentiation. In order to obtain explicit solutions, irrespective of the relative position and orientation of Ω_p in R, Nemat-Nasser and Hori [44] proposed the use of average field quantities. Hence, the volume averages of the perturbation strains taken over Ω_p and R can be expressed in terms of the average eigenstrains as follows [44]:

$$\langle \boldsymbol{\varepsilon}^d \rangle_p = \frac{1}{\Omega_p} \int_{\Omega_p} \int_{\Omega_p} \Gamma(x-y) : \boldsymbol{\varepsilon}^*(y) \mathrm{d}V_y \mathrm{d}V_x = \mathbf{S}_p : \langle \boldsymbol{\varepsilon}^* \rangle_p + \left(\mathbf{S}_R - \mathbf{S}_p \right) : \langle \boldsymbol{\varepsilon}^* \rangle_i \tag{7}$$

where $\mathbf{S}_R$ and $\mathbf{S}_p$ are the Eshelby's tensors of the double inclusions and particles (see references [46–48] for further information on their definition). Using the rule of mixtures, one may write:

$$\langle \boldsymbol{\varepsilon}^d \rangle_R = \frac{f_p}{f_p + f_i} \langle \boldsymbol{\varepsilon}^d \rangle_p + \frac{f_i}{f_p + f_i} \langle \boldsymbol{\varepsilon}^d \rangle_i \tag{8}$$

$$\langle \boldsymbol{\varepsilon}^* \rangle_R = \frac{f_p}{f_p + f_i} \langle \boldsymbol{\varepsilon}^* \rangle_p + \frac{f_i}{f_p + f_i} \langle \boldsymbol{\varepsilon}^* \rangle_i \tag{9}$$

and considering $\langle \boldsymbol{\varepsilon}^d \rangle_R = \mathbf{S}_R : \langle \boldsymbol{\varepsilon}^* \rangle_R$, one can write:

$$\langle \boldsymbol{\varepsilon}^d \rangle_R = \mathbf{S}_R : \left(\frac{f_p}{f_p + f_i} \langle \boldsymbol{\varepsilon}^* \rangle_p + \frac{f_i}{f_p + f_i} \langle \boldsymbol{\varepsilon}^* \rangle_i \right) \tag{10}$$

Now, substituting Eqs. (9) and (10) into Eq. (8), one arrives at:

$$\langle \boldsymbol{\varepsilon}^d \rangle_i = \mathbf{S}_R : \langle \boldsymbol{\varepsilon}^* \rangle_R + \frac{f_p}{f_i} \left(\mathbf{S}_R - \mathbf{S}_p \right) \left(\langle \boldsymbol{\varepsilon}^* \rangle_p - \langle \boldsymbol{\varepsilon}^* \rangle_i \right) \tag{11}$$

Hence, if the eigenstrain field $\boldsymbol{\varepsilon}^*(x)$ produces perturbation strain fields, the following average consistency conditions can be stated:

$$\mathbf{C}_m : \left(\boldsymbol{\varepsilon}^{\mathrm{o}} + \langle \boldsymbol{\varepsilon}^d(x) \rangle - \langle \boldsymbol{\varepsilon}^*(x) \rangle \right) = \begin{cases} \mathbf{C}_p : \left(\boldsymbol{\varepsilon}^{\mathrm{o}} + \langle \boldsymbol{\varepsilon}^d \rangle_p \right), & \forall x \in \Omega_p \\ \mathbf{C}_i : \left(\boldsymbol{\varepsilon}^{\mathrm{o}} + \langle \boldsymbol{\varepsilon}^d \rangle_i \right), & \forall x \in \Omega_i \end{cases} \tag{12}$$

By substituting Eqs. (7) and (11) into Eq. (12), one can get:

$$\boldsymbol{\varepsilon}^{\mathrm{o}} + \left(\mathbf{S}_p + \mathbf{A}_p \right) : \langle \boldsymbol{\varepsilon}^* \rangle_p + \boldsymbol{\Delta S} : \langle \boldsymbol{\varepsilon}^* \rangle_i = \mathbf{0} \tag{13}$$

$$\boldsymbol{\varepsilon}^{\mathrm{o}} + (\mathbf{S}_R + \mathbf{A}_i) : \langle \boldsymbol{\varepsilon}^* \rangle_p + \frac{f_p}{f_i} \boldsymbol{\Delta S} : \left(\langle \boldsymbol{\varepsilon}^* \rangle_p - \langle \boldsymbol{\varepsilon}^* \rangle_i \right) = \mathbf{0} \tag{14}$$

with:

$$\boldsymbol{\Delta S} = \boldsymbol{S}_R - \boldsymbol{S}_p \tag{15}$$

$$\mathbf{A}_p = \left(\mathbf{C}_p - \mathbf{C}_m \right)^{-1} : \mathbf{C}_m \tag{16}$$

$$\mathbf{A}_i = (\mathbf{C}_i - \mathbf{C}_m)^{-1} : \mathbf{C}_m \tag{17}$$

By solving together Eqs. (13) and (14), one may obtain $\langle \boldsymbol{\varepsilon}^* \rangle_p = \boldsymbol{\Phi}_p : \bar{\boldsymbol{\varepsilon}}$ and $\langle \boldsymbol{\varepsilon}^* \rangle_i = \boldsymbol{\Phi}_i : \bar{\boldsymbol{\varepsilon}}$ with:

$$\boldsymbol{\Phi}_p = -\left[\mathbf{S}_p + \mathbf{A}_p + \boldsymbol{\Delta S} : \left(\mathbf{S}_p + \mathbf{A}_p - \frac{f_p}{f_i} \boldsymbol{\Delta S} \right) : \left(\mathbf{S}_p + \mathbf{A}_i - \frac{f_p}{f_i} \boldsymbol{\Delta S} \right)^{-1} \right]^{-1} \tag{18}$$

$$\boldsymbol{\Phi}_i = -\left[\boldsymbol{\Delta S} + \left(\mathbf{S}_p + \mathbf{A}_p \right) : \left(\mathbf{S}_p + \mathbf{A}_p - \frac{f_p}{f_i} \boldsymbol{\Delta S} \right)^{-1} : \left(\mathbf{S}_p + \mathbf{A}_i - \frac{f_p}{f_i} \boldsymbol{\Delta S} \right) \right]^{-1} \tag{19}$$

Now, the strain in the particle and interphase phases can be written as:

$$\bar{\boldsymbol{\varepsilon}}_p = \boldsymbol{\varepsilon}^{\mathrm{o}} + \langle \boldsymbol{\varepsilon}^d \rangle_p = \mathbf{A}_p^{dil} : \boldsymbol{\varepsilon}^{\mathrm{o}} \tag{20}$$

$$\bar{\boldsymbol{\varepsilon}}_i = \boldsymbol{\varepsilon}^{\mathrm{o}} + \langle \boldsymbol{\varepsilon}^d \rangle_i = \mathbf{A}_i^{dil} : \boldsymbol{\varepsilon}^{\mathrm{o}} \tag{21}$$

with:

$$\mathbf{A}_p^{dil} = \mathbf{I} + \mathbf{S}_p : \boldsymbol{\Phi}_p + \boldsymbol{\Delta S} : \boldsymbol{\Phi}_i \tag{22}$$

$$\mathbf{A}_i^{dil} = \mathbf{I} + \mathbf{S}_R : \boldsymbol{\Phi}_i + \frac{f_p}{f_i} \boldsymbol{\Delta S} : \left(\boldsymbol{\Phi}_p - \boldsymbol{\Phi}_i \right) \tag{23}$$

where $\mathbf{A}_i^{dil}$ and $\mathbf{A}_p^{dil}$ denote the concentration factors for interphases and particles in the dilute regime, respectively. Hence, the strain tensors in the particle and interphase phases of Eqs. (20) and (21) can be rewritten as:

$$\bar{\boldsymbol{\varepsilon}}_p = \mathbf{A}_p^{dil} : \left(f_m \mathbf{I} + f_i \mathbf{A}_i^{dil} + f_p \mathbf{A}_p^{dil} \right)^{-1} : \boldsymbol{\varepsilon}^{\mathrm{o}} = \mathbf{A}_p : \boldsymbol{\varepsilon}^{\mathrm{o}} \tag{24}$$

$$\bar{\boldsymbol{\varepsilon}}_i = \mathbf{A}_i^{dil} : \left(f_m \mathbf{I} + f_i \mathbf{A}_i^{dil} + f_p \mathbf{A}_p^{dil} \right)^{-1} : \boldsymbol{\varepsilon}^{\mathrm{o}} = \mathbf{A}_i : \boldsymbol{\varepsilon}^{\mathrm{o}} \tag{25}$$

Here, $\mathbf{A}_i$ are the strain concentration tensors. Finally, the effective moduli of the three-phase composite can be obtained from Eqs. (3) and (4) as follows:

$$\overline{\mathbf{C}} = \left(f_m \mathbf{C}_m + f_i \mathbf{C}_i : \mathbf{A}_i + f_p \mathbf{C}_p : \mathbf{A}_p \right) : \left(f_m \mathbf{I} + f_i \mathbf{A}_i + f_p \mathbf{A}_p \right)^{-1} \tag{26}$$

Let us note that Eq. (26) is in general orientation dependent. In order to describe the orientation of fillers, a reference local coordinate system $\mathrm{K}' \equiv \left\{ 0; x_1' x_2' x_3' \right\}$ is fixed in each particle. In this paper, it is assumed that all the inclusions are monodispersed and defined as ellipsoids with an aspect ratio $(1, 1, \kappa)$, being the major axis aligned in the local x_3' direction as indicated in Fig. 2. Due to the rotational symmetry of the defined ellipsoidal inclusions, only two Euler angles, θ and γ, are required to describe the relative orientation of any orthogonal coordinate system with respect to the global one, $\mathrm{K} \equiv \{0; x_1 x_2 x_3\}$. Hence, the coordinate transformation of a fourth-rank tensor $\mathbf{P}$ into the local coordinate system K' is explicitly represented in terms of the transformation matrix $\mathbf{g}$ as:

$$P'_{ijlk} = g_{ip}g_{jq}g_{kr}g_{ls}P_{pqrs} \tag{27}$$

Due to the high number of fillers contained in the RVE, the description of their orientation field is of statistical nature. The probability of a particle lying in an infinitesimal range of angles $[\theta, \theta + \mathrm{d}\theta]$, and $[\gamma, \gamma + \mathrm{d}\gamma]$ is given by $\Omega(\theta, \gamma)\sin(\theta)\mathrm{d}\theta\mathrm{d}\gamma$, with $\Omega(\theta, \gamma)$ being the so-called Orientation Distribution Function (ODF). Any ODF must satisfy the following normalization condition:

$$\int_0^{2\pi}\int_0^{\pi/2} \Omega(\theta, \gamma)\sin(\theta)\mathrm{d}\theta\mathrm{d}\gamma = 1 \tag{28}$$

in which for the particular case of randomly oriented inclusions, it can be seen that $\Omega(\theta, \gamma) = 1/2\pi$. The integration of any ODF weighted function $F(\theta, \gamma)$ over all possible orientations in the Euler space, also referred to as the orientational average of F, $\{F\}$, is defined through:

$$\{F\} = \int_0^{2\pi}\int_0^{\pi/2} F(\theta, \gamma)\Omega(\theta, \gamma)\sin(\theta)\mathrm{d}\theta\mathrm{d}\gamma \tag{29}$$

On this basis, Eq. (26) can be rewritten for random filler configurations as:

$$\overline{\mathbf{C}} = \left(f_m\mathbf{C}_m + f_i\left\{\mathbf{C}_i : \mathbf{A}_i\right\} + f_p\left\{\mathbf{C}_p : \mathbf{A}_p\right\}\right) : \left(f_m\mathbf{I} + f_i\left\{\mathbf{A}_i\right\} + f_p\left\{\mathbf{A}_p\right\}\right)^{-1} \tag{30}$$

Finally, the volume fraction of the interphases remains to be defined according to their behavior, including hard or soft interphases as shown in Fig. 3. In general, a hard interface zone is one that possesses a high stiffness and can be considered as impenetrable layers surrounding the particles. Conversely, compliant interface zones typically possess low stiffness and can be considered as penetrable layers surrounding the particles. For hard interphases, Fig. 3 (a), their volume fraction is directly related to the number density of ellipsoidal particles and the interphase volume. Assuming that the interphases are defined by a constant thickness t around the particles, Xu *et al*. [17] derived the expression of the volume fraction of hard interfaces around monodisperse ellipsoidal particles as:

$$f_i = 6f_p\left[\frac{\lambda}{n(\kappa)} + \Omega(\kappa)\lambda^2 + \frac{4}{3}\lambda^3\right] \tag{31}$$

where λ is the ratio of the interfacial thickness t and the particle size D_{eq} (i.e. $\lambda = t/D_{eq}$). The equivalent diameter D_{eq} is defined as the diameter of a sphere having the same volume as that of an ellipsoidal particle [49]. Considering that particles have a minor axis D, the equivalent diameter is defined as $D_{eq} = D\kappa^{-2/3}$ for $\kappa \leq 1$ or $D_{eq} = D\kappa^{1/3}$ for $\kappa \geq 1$. The term $n(\kappa)$ is the sphericity of an ellipsoidal particle with aspect ratio κ, and is defined as the ratio between the surface area of a sphere and the ellipsoid with the same volume, that is:

$$n(\kappa) = \begin{cases} \frac{2\kappa^{2/3}\sin\varphi}{\sin\varphi + \kappa^2\,\mathrm{arctanh}(\sin\varphi)}, & \kappa < 1 \quad \text{(Oblate particles)} \\ 1, & \kappa = 1 \quad \text{(Spherical particles)} \\ \frac{2\kappa^{2/3}\tan\varphi}{\tan\varphi + \kappa^2\varphi}, & \kappa > 1 \quad \text{(Prolate particles)} \end{cases} \tag{32}$$

where φ is defined as $\varphi = \arccos(\beta)$, with $\beta = 1/\kappa$ for $\kappa \geq 1$ or $\beta = \kappa$ for $\kappa \leq 1$. The term $\Omega(\kappa)$ is a specific function on κ defined as:

$$\Omega(\kappa) = \begin{cases} \kappa^{2/3} + \frac{\ln\left(\kappa + \sqrt{\kappa^2 - 1}\right)}{\kappa^{1/3}\sqrt{\kappa^2 - 1}}, & \kappa < 1 \\ 2, & \kappa = 1 \\ \kappa^{2/3} + \frac{\sin^{-1}\sqrt{1-\kappa^2}}{\kappa^{1/3}\sqrt{1-\kappa^2}}, & \kappa > 1 \end{cases} \tag{33}$$

Finally, Xu *et al*. [43] derived the volume fraction of soft interphases around monodisperse ellipsoidal particles as:

$$\begin{aligned} f_i = (1 - f_p)\Bigg(1 - \exp\Bigg\{-\frac{6f_p}{1 - f_p}\left[\frac{\lambda}{n(\kappa)} + \left(2 + \frac{3f_p}{n^2(\kappa)(1 - f_p)}\right)\lambda^2 + \right. \\ \left. + \frac{4}{3}\left(1 + \frac{3f_p}{n(\kappa)(1 - f_p)} + \frac{mf_p^2}{n^3(\kappa)(1 - f_p)^2}\right)\lambda^3\right]\Bigg\}\Bigg) \end{aligned} \tag{34}$$

where parameter m controls the theoretical approximation of the radial distribution function of spherical particle systems. Xu *et al*. [43] demonstrated that vales of m=0, 2 and 3 yield identical results and, therefore, $m = 0$ is used in this work.

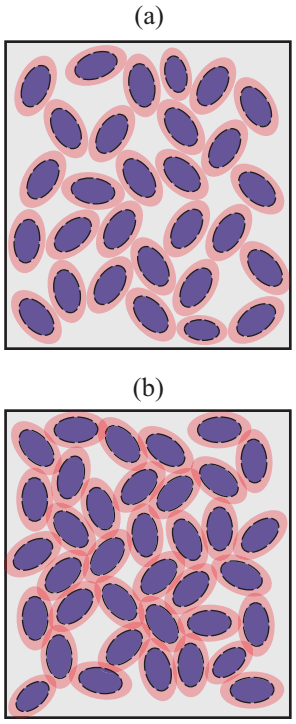

Figure 3: Schematics for three-phase composite structures with reinforcing particles, matrix and (a) hard impenetrable interphases or (b) soft penetrable interphases.

Let us finally note that the previously overviewed formulation is general for any monodisperse particle-reinforced composites. Different geometries of interphases can be implemented through Eq. (15) and an adequate definition of the particle interphase volume fraction, as well as diverse matrix materials through an appropriate implementation of the Eshelby's tensors and the constitutive tensors.

2.2. Step I.B: Partially saturated voids

In order to take into account the effects of the saturation degree, non-connected partially saturated pores can be replaced by equivalent homogeneous inclusions as sketched in Fig. 4. To this end, the equivalent modulus can be estimated through the Voigt approximation (iso-deformation hypothesis) or the Reuss approximation (iso-stress hypothesis) [42, 50]. On the basis of the hypothesis of uniform fluid pressure, the Reuss approximation has been reported to be more appropriate [50], whereby the bulk modulus of the equivalent homogeneous pores accordingly writes:

$$\frac{1}{K_{ep}} = \frac{S}{K_w} + \frac{1-S}{K_v} \tag{35}$$

where S stands for the degree of water saturation, K denotes bulk modulus, and subscripts v, w and ep refer to void, water and equivalent pore phases, respectively. Fig. 5 plots the bulk modulus of partially saturated pores K_{ep} as a function of the saturation degree S. Let us indicate that the bulk modulus of the liquid phase is selected as K_w=2.3 GPa, while the gas phase is defined with a very small bulk modulus of K_v=0.013 GPa. It can be seen in this figure that the bulk modulus of the equivalent pores increases slowly with the degree of water saturation until around $S = 0.8$, followed by a sharp increase until the situation of fully saturated pores.

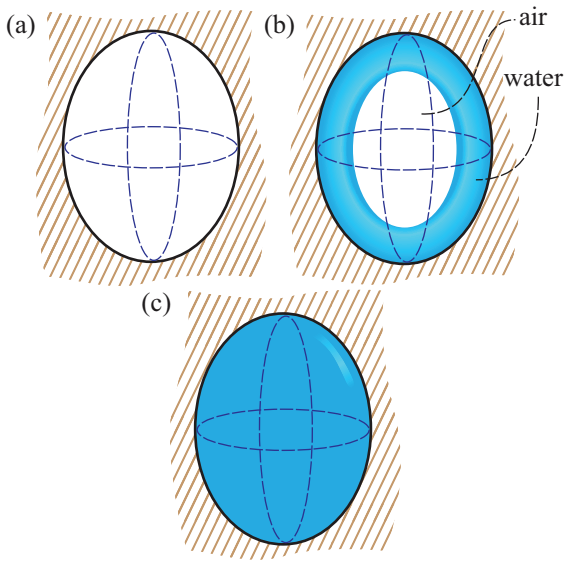

Figure 4: Water and gas in pores: (a) dry pore, (b) unsaturated pore and (c) saturated pore.

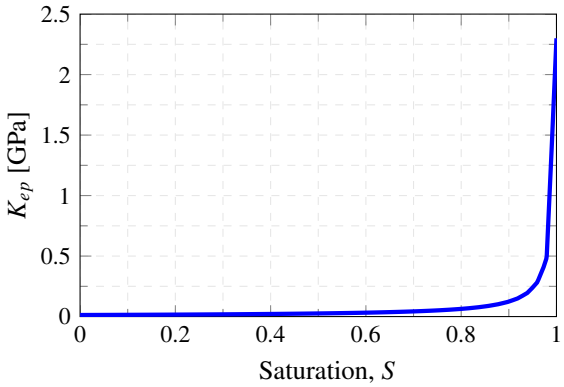

Figure 5: Effective bulk modulus K_{ep} as a function of saturation S for partially saturated porous media (K_v=0.013 GPa, K_w=2.3 GPa).

2.3. Step II: Particle-reinforced porous composites

In order to incorporate porosity into the modeling of particle-reinforced composites with interface effects, a two-step hierarchical homogenization approach is developed as illustrated in Fig. 6. In the first step, Step I.A, the homogenization procedure presented in Section 2.1, Eq. (30), is used to evaluate the effective elastic moduli of the three-phase composite, $\overline{\mathbf{C}}_m$, which consists of the matrix material, particles and interphases with constitutive tensors $\mathbf{C}_m$, $\mathbf{C}_p$, and $\mathbf{C}_i$, respectively. Moreover, the homogenization approach presented in Section 2.2 is employed to obtain the equivalent homogeneous properties of partially saturated pores, $\mathbf{C}_v$. Finally, Step II comprises the homogenization of a two-phase composite, including matrix and ellipsoidal inclusion phases with elastic moduli given by the previously computed constitutive tensors $\overline{\mathbf{C}}_m$ and $\mathbf{C}_v$, respectively. In this step, the inclusion volume fraction is defined by the porosity, ϕ. Therefore, the overall constitutive tensor of the composite, $\overline{\mathbf{C}}$, can be directly obtained by the Mori-Tanaka model as follows:

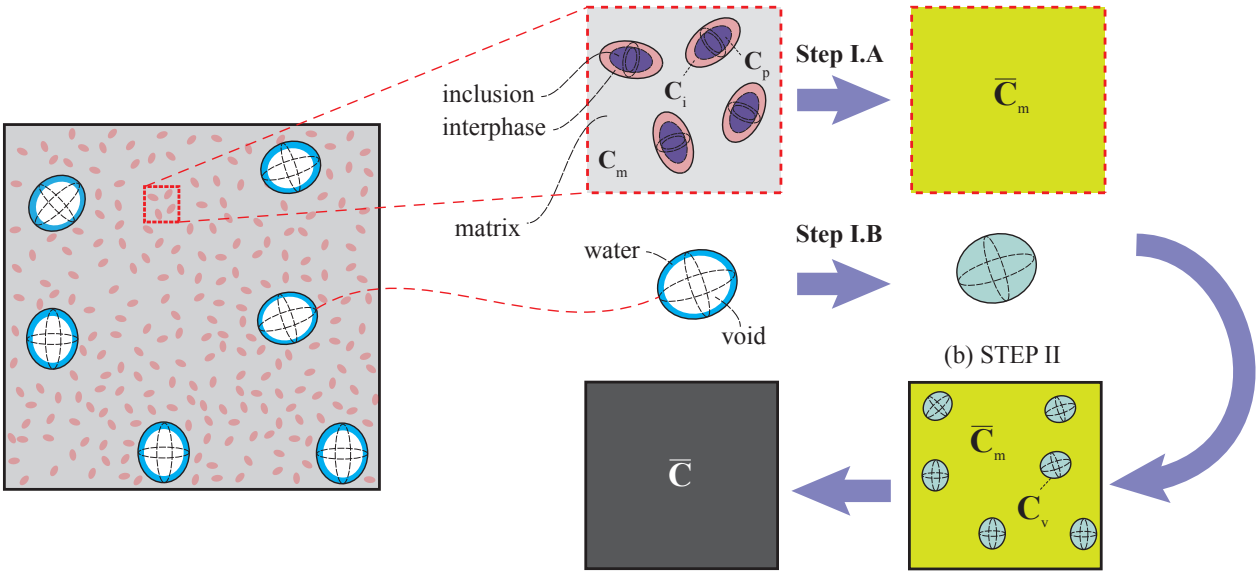

Figure 6: Schematic diagram of the proposed two-step hierarchical micromechanics model for particle-reinforced porous composites with interface effects.

$$\overline{\mathbf{C}} = \left((1-\phi)\overline{\mathbf{C}}_m + \phi\left\{\mathbf{C}_v\mathbf{A}_v^{dil}\right\}\right) : \left((1-\phi)\mathbf{I} + \phi\left\{\mathbf{A}_v^{dil}\right\}\right)^{-1} \tag{36}$$

where $\mathbf{A}_v^{dil}$ is the dilute strain concentration tensor for pore inclusions and is given by:

$$\mathbf{A}_v^{dil} = \left[\mathbf{I} + \mathbf{S}_v : \left(\overline{\mathbf{C}}_m\right)^{-1} : \left(\mathbf{C}_v - \overline{\mathbf{C}}_m\right)\right]^{-1} \tag{37}$$

with $\mathbf{S}_v$ being the Eshelby's tensor of pores, which controls their geometry given by the pore aspect ratio κ_ϕ. For illustrative purposes, Fig. 7 furnishes the effective shear $\overline{\mu}$ and bulk $\overline{K}$ moduli of dry porous isotropic media as a function of the porosity ϕ. In this case, pores are full of air and simply act as voids with bulk modulus K_v=0.013 GPa and negligible shear modulus μ_v=0.0 GPa. As an example, the matrix bulk and shear moduli are assumed as K_m=63.30 GPa and μ_m=17.10 GPa, and the pores are defined as spherical inclusions ($\kappa_\phi = 1$). It is observed in this figure that the effective elastic moduli substantially decrease with the increase in porosity and, therefore, these results highlight the weakening effect of porosity on the overall stiffness of porous composites.

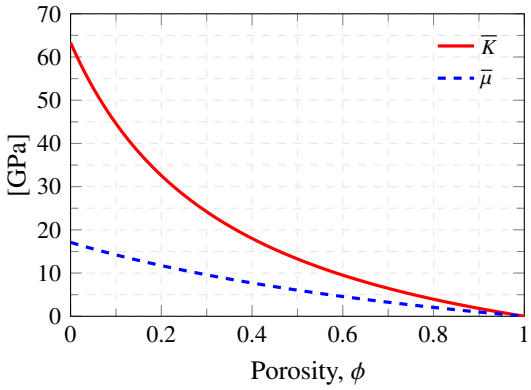

Figure 7: Effective shear $\overline{\mu}$ and bulk $\overline{K}$ moduli as functions of porosity for porous media containing voids (K_m=63.30 GPa, μ_m=17.10 GPa, K_v=0.013 GPa, μ_v=0.0 GPa, κ_ϕ=1).

Fig. 8 depicts the effective bulk modulus of unsaturated porous media versus the saturation degree. The elastic bulk modulus of the water phase is assumed to be K_w=2.3 GPa, and its shear modulus is neglected μ_w=0.0 GPa. Three different porosity levels are selected, namely ϕ=0.50, 0.55 and 0.60. As expected from previous analyses, lower porosity contents yield higher stiffness values. With regard to the saturation degree, it is also noted that only

slight variations are found for saturation degrees below approximately 0.8, whilst the overall stiffness experiences rapid increases for higher saturation degrees up to the limit condition of saturated porosity, $S = 1$.

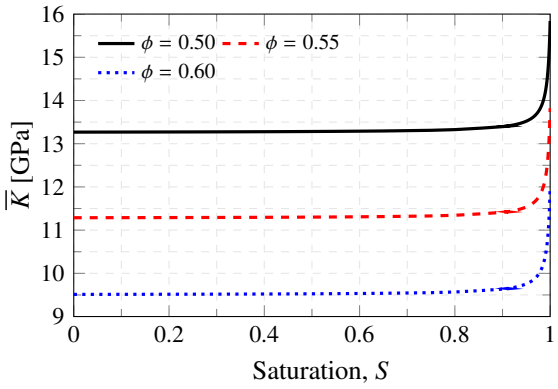

Figure 8: Effective bulk modulus $\overline{K}$ versus saturation degree for partially saturated porous media (K_m=63.30 GPa, μ_m=17.10 GPa, K_v=0.013 GPa, μ_v=0.0 GPa, K_w=2.3 GPa, μ_w=0.0 GPa, κ_ϕ=1).

3. Numerical results and discussion

This section presents a set of numerical results to evaluate the validity and effectiveness of the proposed two-step hierarchical micromechanics approach for the modeling of unsaturated porous composites doped with monodisperse particles with interface properties. The numerical tests are categorized into three subsections: Subsections 3.1 and 3.2 investigate the elastic moduli of particle-reinforced composites with hard and soft interphases, respectively, and Subsection 3.3 presents parametric analyses for particle-reinforced porous composites.

3.1. Particulate composites with hard interfaces

This first set of tests is intended to demonstrate the capabilities of the presented micromechanics approach for predicting the mechanical properties of nano-modified composites with hard interphases. In particular, the experimental results provided by Carballeira and Haupert [51] on the mechanical properties of epoxy resin doped with titanium dioxide (TiO_2) have been used as validation basis. Both the matrix and reinforcing phases are assumed isotropic with elastic moduli E_m=2436 MPa and E_p=283 GPa, and Poisson's ratios ν_m=0.35 and ν_p=0.28 [27, 51]. Fig. 9 shows the comparison of the experimental data against the theoretical estimates. The results are furnished in non-dimensional form through the stiffening efficiency of the particles, that is, the ratio between the Young's moduli of the resulting composite $\overline{E}$ and the matrix E_m. For illustrative purposes, the predictions disregarding the interphase regions, that is to say, the estimates provided by the conventional two-phase Mori-Tanaka model, are depicted with dashed lines. It is noted that the latter approach substantially underestimates the experimental results and, therefore, this fact evidences the existence of interphase regions with stiffer properties than the hosting matrix material. In this case, the interfacial characteristics are defined at the nano-scale by means of certain interatomic potentials between the inclusions and the surrounding matrix. The characterization of such interactions would require the use of sophisticated experimental techniques such as nano-indentation or Scanning Electron Microscopy (SEM), or computationally demanding atomistic-based simulations. For the sake of simplicity, the thickness t and elastic modulus E_i of the interphase regions have been estimated through a Least Squares Nonlinear Regression (LSNR) of the proposed approach with respect to the experimental data. As a result, values of t=24 nm E_i=44.38 GPa have been obtained. It can be observed in Fig. 9 that the estimates of the present approach with fitted interphase parameters are in very close agreements with the experimental data. As a conclusion, these results demonstrate the key role of the interfacial effects on the overall elastic moduli of nano-sized particle-reinforced composites.

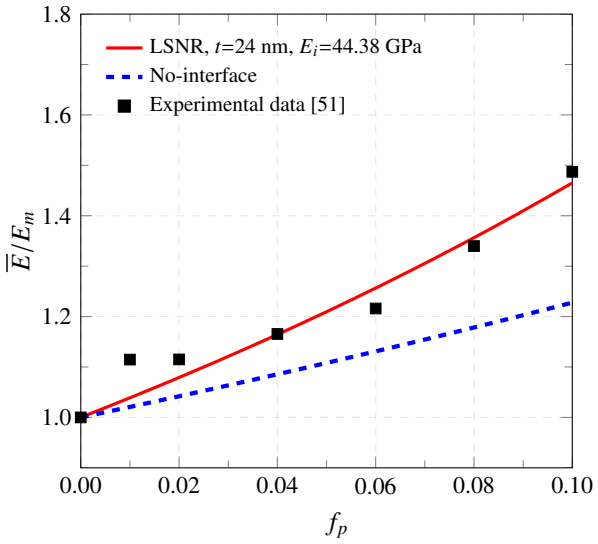

Figure 9: Prediction of the stiffening efficiency $\overline{E}/E_m$ of epoxy resin doped with TiO_2 nanoparticles versus the filler volume fraction f_p (D_{eq}=200 nm, κ=1.0, E_m=2436 MPa, ν_m=0.35, E_p=283 GPa, ν_p=0.28, LSNR stands for the least squares nonlinear regression of the present approach with respect to the experimental data).

In order to give some insight into the structure of the presented approach, Figs. 10 (a) and (b) investigate the effect of the particle-to-matrix stiffness E_i/E_m and thickness-to-particle size $\lambda = t/D_{eq}$ ratios, respectively. In the first analysis in Fig. 10 (a), λ is fixed at 0.5, and values of 0.1, 0.5, 2.0 and 3.0 are chosen for E_i/E_m. It is observed that the particle stiffening efficiency dramatically increases when $E_i/E_m > 1$, that is to say, when the interphases are stiffer than the matrix. In the particular case of E_i/E_m=1.0, the model degenerates into the standard two-phase Mori-Tanaka model. Conversely, when $E_i/E_m < 1$, the interphases are less stiff than the matrix material and, therefore, the stiffening efficiency decreases. On the other hand, Fig. 10 (b) analyzes the effect of λ when E_i/E_m is fixed at 6.38. In particular, values of $\lambda = t/D_{eq} = 0.05$, 0.10, 0.15, and 0.20 are chosen. According to Eq. (31), the volume fraction of hard interphases depends upon the size and aspect ratio of the inclusions. Then, given that in this case the interphases have been assumed to be stiffer than the matrix material, as λ increases, so does the particle stiffening efficiency E_i/E_m. It is also noted that, when the thickness of the interphases approaches 0, so does λ and the model degenerates into the classical two-phase Mori-Tanaka approach. The effect of the particle volume fraction f_p on the interphase volume fraction f_i is further investigated in Fig. 11. In a similar way to Fig. 10 (b), different λ ratios are selected. It is clearly observed that the volume fraction of non-overlapping interphases is monotonically increasing with the particle volume fraction. Furthermore, higher λ ratios imply thicker interphases and, therefore, higher interphase volume fractions. As a consequence, the macroscopic elastic modulus increases more rapidly with the filler content for larger interphase thicknesses, what gives an explanation to the previous results in Fig. 10 (a).

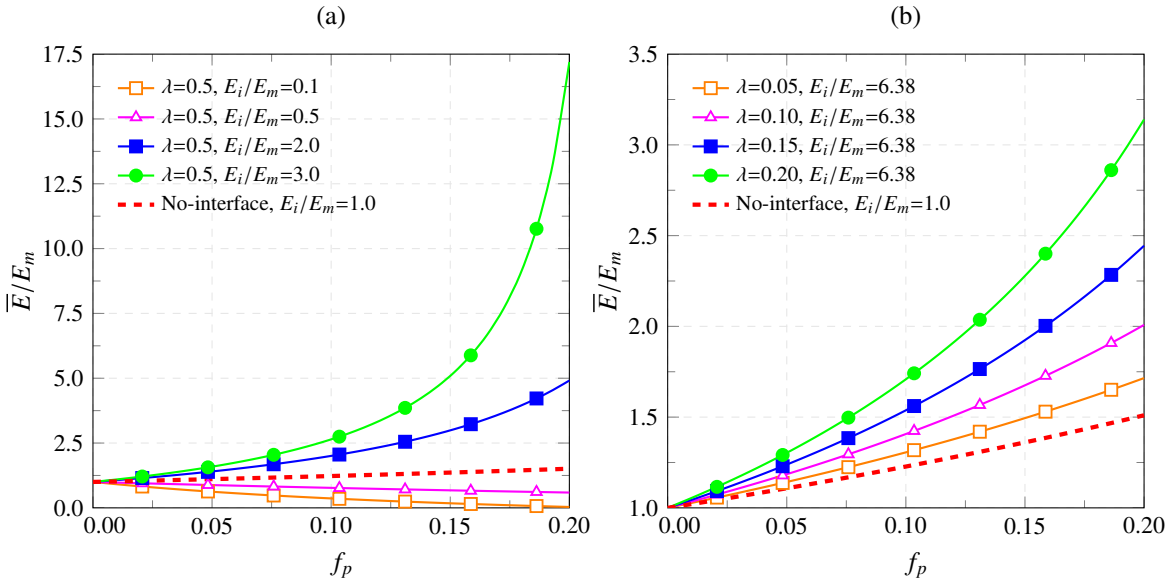

Figure 10: Stiffening efficiency $\overline{E}/E_m$ of epoxy resin doped with TiO_2 nanoparticles with varying E_i/E_m (a) and $\lambda = t/D_{eq}$ (b) ratios (D_{eq}=200 nm, κ=1.0, E_m=2436 MPa, ν_m=0.35, ν_p=0.28).

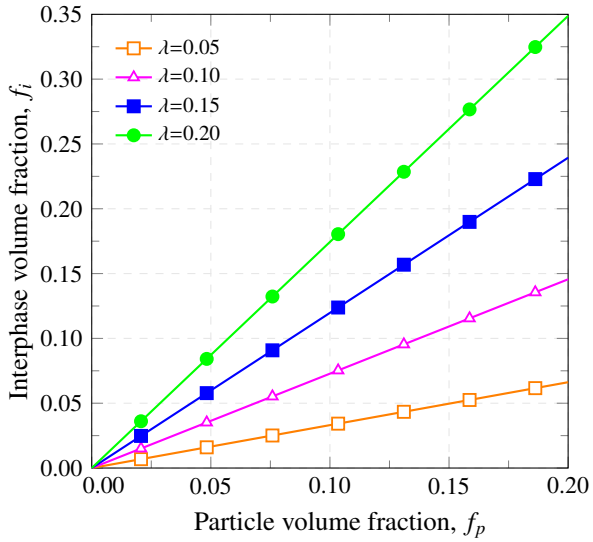

Figure 11: Volume fraction of hard interphases f_i versus volume fraction of particles f_p with different $\lambda = t/D_{eq}$ ratios (D_{eq}=200 nm, κ=1).

Finally, the effect of the particle-to-matrix stiffness ratio E_p/E_m on the particle stiffening efficiency $\overline{E}/E_m$ of epoxy/TiO_2 is analyzed in Fig. 12. First, different particle volume fractions f_p are considered in Fig. 12 (a). It is noted that the differences between the present three-phase approach and the two-phase Mori-Tanaka model (plotted with dashed lines) get consistently reduced with lower particle contents. In this figure, two major regions can be distinguished as follows. The first region comprises low E_p/E_m ratios, and $\overline{E}/E_m$ is shown to be continuously increasing until it reaches an asymptotic limit. In the second region, defined by high E_p/E_m ratios, only slight increases in $\overline{E}/E_m$ are observed. The influence of the filler aspect ratio κ on the macroscopic elastic modulus is also studied in Fig. 12 (b). In this case, the filler content is fixed at $f_p = 5\%$, and oblate ($\kappa < 1$) and prolate ($\kappa > 1$) ellipsoidal particles are investigated. Both oblate and prolate particles tend to an asymptotic limit as the ratio E_p/E_m increases. Furthermore, it is noted that spherical particles lead to the lowest stiffening efficiencies.

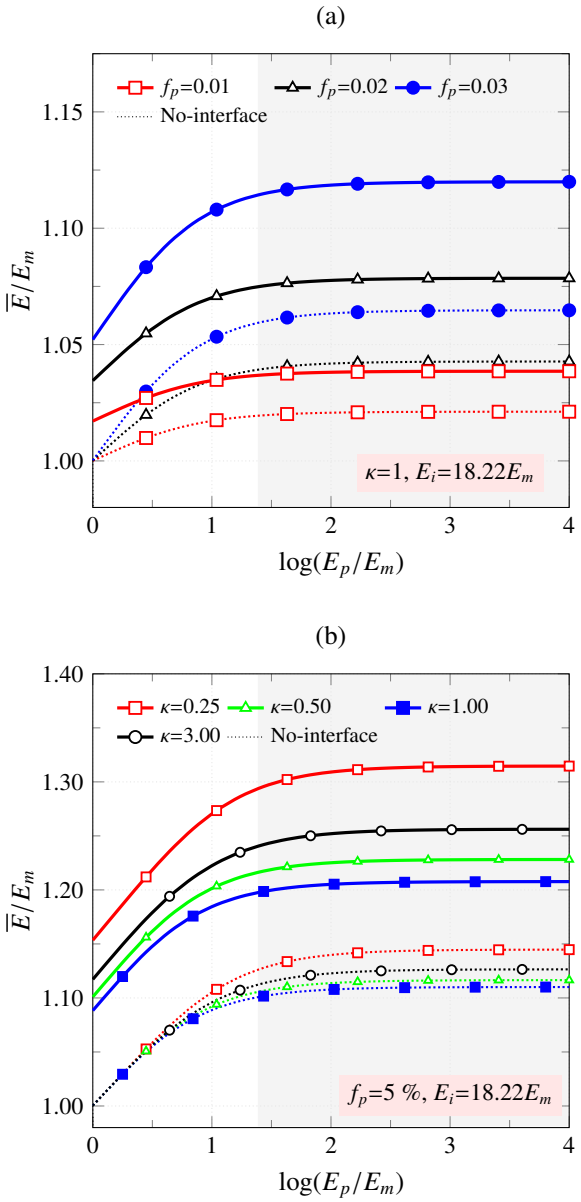

Figure 12: Stiffening efficiency $\overline{E}/E_m$ versus particle to matrix stiffness ratio E_p/E_m for varying filler volume fraction f_p (a), and filler aspect ratio κ (b) (t = 24 nm, D_{eq}=200 nm, E_m=2436 MPa, ν_m=0.35, ν_p=0.28).

3.2. Particulate composites with soft interfaces

In this second set of tests, particle-reinforced composites with overlapping interphases are studied with the proposed micromechanics approach. Firstly, the experimental results reported by Yang [26] on the elastic properties of normal concrete have been selected as validation benchmark. The Young's modulus of cement paste is E_m=20.76 GPa and its Poisson's ratio ν_m = 0.2 , whilst the Young's modulus of the aggregates is E_p = 80 GPa and its Poisson's ratio ν_p = 0.21 [26]. In a similar way to the previous analysis, Fig. 13 depicts the comparison of the experimental data against the theoretical estimates with and without interface effects. In this case, it is noted that the two-phase Mori Tanaka model (estimates disregarding the interface effects) overestimates the experimental data. This circumstance evidences the existence of Interfacial Transition Zones (ITZs) that weaken the overall stiffness of the particulate system, that is, soft interphases. The origin of these regions lies in the packing of the cement grains against aggregates, and such regions are characterized by a local increase in porosity and smaller cement particles. Due to the difficulty in obtaining the elastic properties of ITZs, the proposed micromechanics approach has been fitted by LSNR, leading to values of interphase thickness of t=69 μm, and interphase Young's modulus of E_i=14.42 GPa which, indeed, is around one fifth of the Young's modulus of the aggregates. Using these fitted interphase parameters, very close agreements can be observed between the theoretical and experimental data.

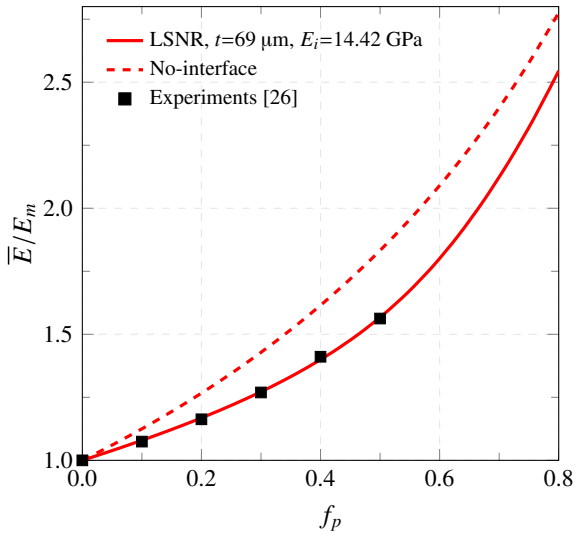

Figure 13: Prediction on the stiffening efficiency $\overline{E}/E_m$ of concrete with interface effects (D_{eq}=450 μm, κ=1.0, E_m=20.76 GPa, ν_m=0.20, E_p=80 GPa, ν_p=0.21, LSNR stands for the least squares nonlinear regression of the present approach with respect to the experimental data).

The influence of the filler aspect ratio κ on the particle stiffening efficiency $\overline{E}/E_m$ of normal concrete with interface effects is investigated in Fig. 14. In addition, different thickness-to-particle size ratios $\lambda = t/D_{eq}$ ranging from 0.1 to 0.5 are included. It is noted that, contrary to the previously reported results in Fig. 12, spherical particles lead to the largest macroscopic stiffness values for every λ ratio. In this case, this behavior finds an explanation in the stiffer properties of the matrix in comparison to the interphase layers ($E_i/E_m = 0.69$). Moreover, it is also observed that higher λ ratios, that is to say, thicker interphases, lead to less stiff composites.

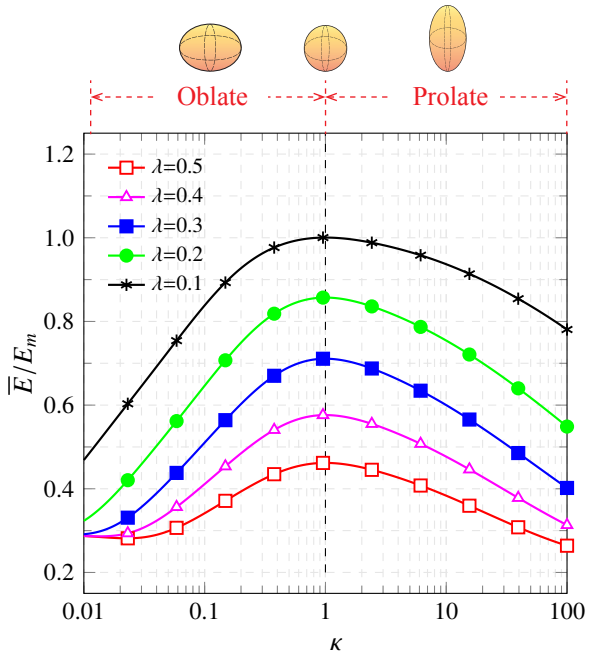

Figure 14: Stiffening efficiency $\overline{E}/E_m$ of concrete with interface effects versus filler aspect ratio κ and varying $\lambda = t/D_{eq}$ ratios (D_{eq}=450 μm, E_m=20.76 GPa, ν_m=0.20, E_p=80 GPa, ν_p=0.21).

Finally, the dependence of the volume fraction of soft interphases f_i on the filler aspect ratio κ and filler content f_p is studied in Figs. 15 (a) and (b), respectively. In the first case in Fig. 15 (a), the filler content is fixed at $f_p = 10\%$ and, in the second case in Fig. 15 (b), it is assumed that particles are spherical inclusions $\kappa = 1$. In both cases, different values of λ are analyzed, namely 0.1, 0.2, 0.3, 0.4 and 0.5. It is noted that, consistently, higher interphase volume fractions are obtained for higher λ ratios or, equivalently, thicker interphases. With regard

to Fig. 15 (a), it is found that the volume fraction of soft interphases f_i exhibits minimum values for spherical particles $\kappa = 1$. In the case of oblate particles $0 < \kappa < 1$, the interphase volume fraction drastically decreases from maximum values corresponding to platelet particles $\kappa \to 0$. Conversely, in the case of prolate particles $\kappa > 1$, only slow increases are found for higher particle aspect ratios. With regard to Fig. 15 (b), it can be observed that the interphase volume fraction increases until a certain particle content where maximum values are registered. Afterward, as the filler content continues to grow, the volume fraction of the interphases decreases until zero where all the volume is occupied by the particles. It is interesting to note that, once the maximum values are reached, all the curves converge to the same straight line corresponding to $f_i + f_p = 1$. At this point, the interphases and particles completely fill the composite, that is, $f_m = 0$, and, as the particle content continues to increase, part of the interphase region begins to be occupied by the particles. Following this reasoning, it can be seen that larger λ ratios reach this saturation point at lower filler contents.

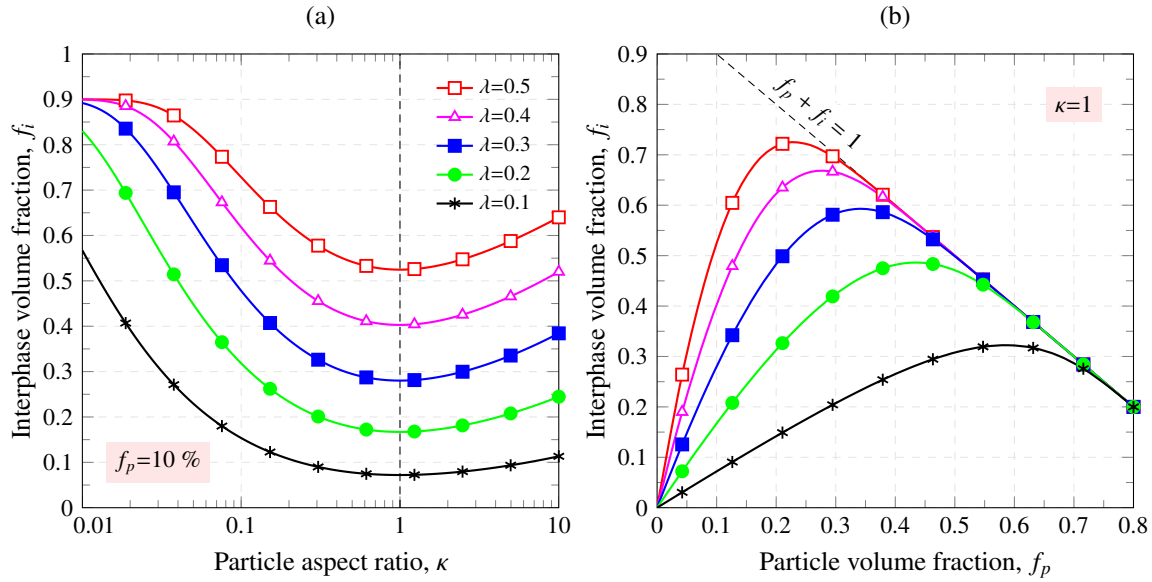

Figure 15: Soft interphase volume fraction f_i versus filler aspect ratio κ (a) and particle volume fraction f_p (b) (D_{eq}=450 μm).

3.3. Particle-reinforced unsaturated porous composites

In this last section, the effective properties of particle-reinforced unsaturated porous composites with interface effects are computed by the proposed two-step hierarchical micromechanics approach as explained in Section 2.3. Firstly, the theoretical estimates of the macroscopic stiffness of porous media are benchmarked against experimental data in Fig. 16. The experimental results reported by Yaman *et al.* [52] on normal concrete has been taken as validation basis. In this case, concrete is assumed to be homogeneous and isotropic with dry and saturated Young's moduli E_m^{dry}=45.35 GPa and $E_m^{saturated}$=46.62 GPa (Table 4 in [52]), respectively, and Poisson's ratio $\nu_m = 0.2$. Three different pore aspect ratios are also selected, namely $\kappa_\phi = 0.3$, 0.4, and 1.0. Experimental results are plotted for both dry and saturated conditions with varying porosity degrees (Table 6 in [52]). It is noted that the results for oblate pores with $\kappa_\phi = 0.4$ fit considerably well the experimental data, although slight discrepancies can be observed for saturated conditions. These differences are ascribed to the consideration in the proposed model of porosity only as entrained pores (non-active pores), disregarding capillary pores (active pores) which would require a more sophisticated poroelastic definition. Overall, it can be extracted from this figure, in accordance with the previously discussed Figs. 7 and 8, that porosity has a substantial weakening effect on the macroscopic stiffness and that saturated composites exhibit slightly stiffer behaviors.

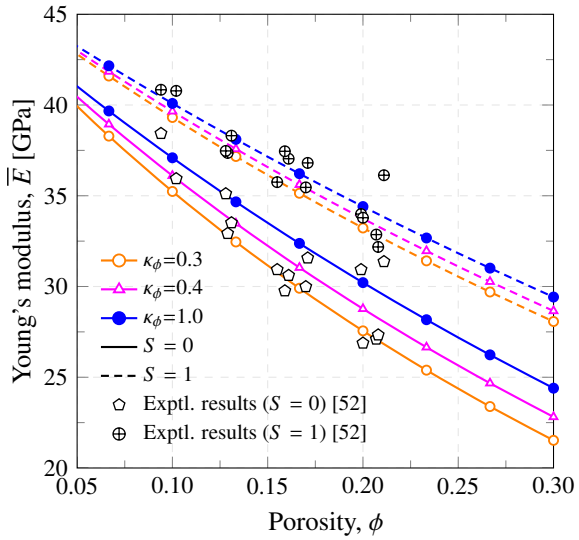

Figure 16: Young's modulus of concrete versus porosity (E_m^{dry}=45.35 GPa, $E_m^{saturated}$=46.62 GPa, ν_m=0.2).

In the remainder of this section, normal concrete is selected for illustrative purposes. In particular, concrete is assumed to be a composite material consisting of cement and aggregates as matrix and particle phase constituents, respectively. The material properties of the different phases have been taken from the previous subsection. The influence of the volume fraction of aggregates f_p on the macroscopic Young's modulus $\overline{E}$ of dry concrete is investigated in Fig. 17. Furthermore, different porosity levels are studied, namely ϕ = 0 (non-porous), 0.1, 0.2, and 0.3. The predictions computed by the conventional two-phase Mori-Tanaka model without interface effects are also depicted with dashed lines. In accordance with the previous results, it is clearly observed that porosity induces substantial softening effects on the macroscopic stiffness. For instance, a porosity value of 30% leads to reductions of the effective Young's modulus up to about 50% for an aggregate volume fraction of 0.8. Furthermore, Figs. 18 (a) and (b) show the effective bulk and shear moduli of dry concrete as a function of porosity with different contents of agglomerates, respectively. Interestingly, it is noted that the interface effects are especially noticeable in the macroscopic shear modulus.

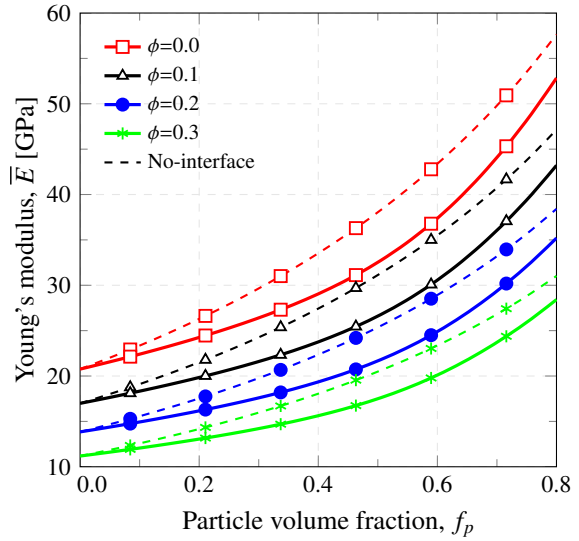

Figure 17: Prediction on the effective Young's modulus $\overline{E}$ of dry concrete with soft interface effects and different porosity values (D_{eq}=450 µm, κ=1.0, E_m=20.76 GPa, ν_m=0.20, E_p=80 GPa, ν_p=0.21, E_i=14.42 GPa, t=69 µm, κ_ϕ = 1.0).

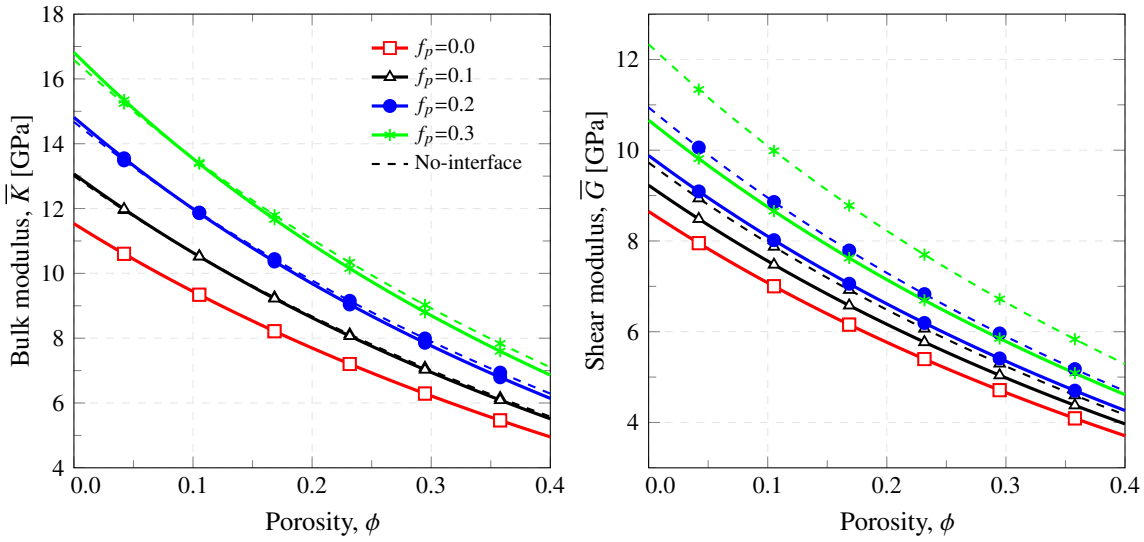

Figure 18: Effective bulk $\overline{K}$ and shear moduli $\overline{G}$ of dry concrete with soft interface effects versus porosity (D_{eq}=450 μm, κ=1.0, E_m=20.76 GPa, ν_m=0.20, E_p=80 GPa, ν_p=0.21, E_i=14.42 GPa, t=69 μm, κ_ϕ = 1.0).

Finally, the effect of water saturation of pores is investigated in Figs. 19 and 20. Firstly, Figs. 19 (a) and (b) depict the macroscopic bulk and shear moduli of unsaturated concrete as a function of the pore aspect ratio κ_ϕ, respectively. In these tests, an aggregate volume fraction of 10% and a porosity of 30% are selected, as well as different saturation levels, namely S = 0.00, 0.80, 0.90 and 0.95. It is first noted that both the overall bulk and shear moduli rapidly decrease for every saturation degree until a pore aspect ratio around 10. Then, the overall stiffness reaches an asymptotic value for increasing pore aspect ratios. With regard to the water saturation degree of pores, only noticeable effects can be found in the macroscopic bulk modulus due to the null shear stiffness of pores. Also, in accordance with the previous results, higher levels of water saturation of the pores lead to a stiffer behavior of the composites. Finally, Fig. 20 furnishes the effective Young's modulus $\overline{E}$ of unsaturated concrete with soft interface effects as a function of the water saturation degree S for different aggregate volume fractions, namely f_p = 0, 1, 3 and 5%. It is first noted that higher volume fractions of aggregates yield larger macroscopic Young's moduli. Moreover, in a similar way to the results previously shown in Fig. 5, the saturation of pores only exhibits significant stiffening effects for saturation degrees above 0.8. For instance, in the case of concretes loaded with 5% of aggregates, the Young's modulus of the saturated system is about 5% higher than that of the dry system.

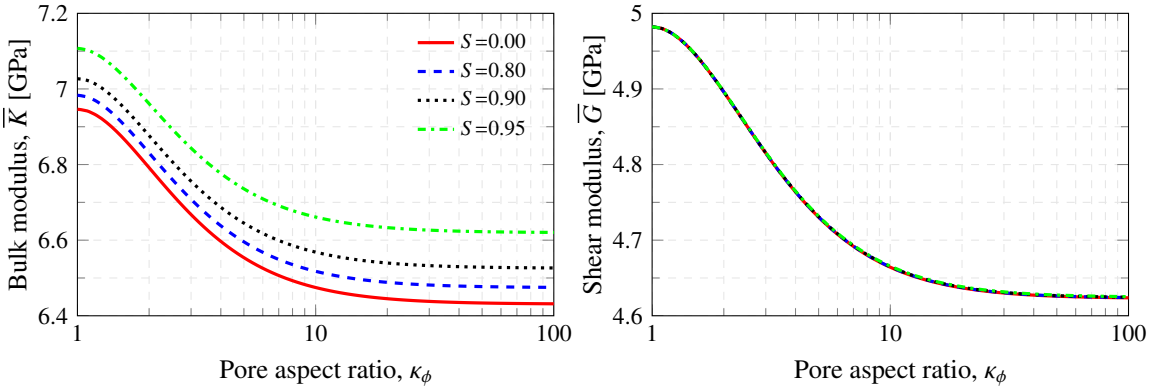

Figure 19: Effective bulk $\overline{K}$ and shear moduli $\overline{G}$ of unsaturated concrete with soft interface effects versus pore aspect ratio κ_p (D_{eq}=450 μm, κ=1.0, E_m=20.76 GPa, ν_m=0.20, E_p=80 GPa, ν_p=0.21, E_i=14.42 GPa, t=69 μm, f_p=10%, ϕ=30%, κ_ϕ = 1.0).

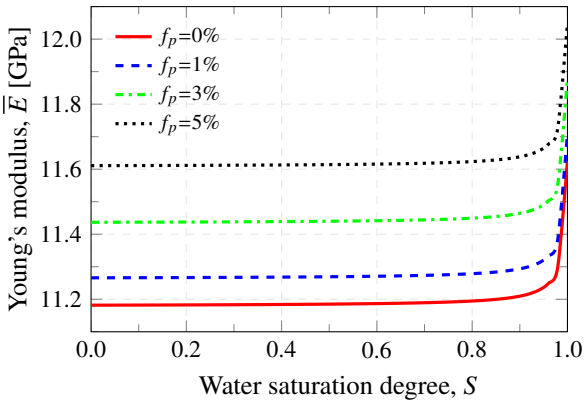

Figure 20: Effective Young's modulus $\overline{E}$ of unsaturated concrete with soft interface effects versus saturation degree S (D_{eq}=450 μm, κ=1.0, E_m=20.76 GPa, ν_m=0.20, E_p=80 GPa, ν_p=0.21, E_i=14.42 GPa, t=69 μm, ϕ=30%, κ_ϕ = 1.0).

4. Conclusions

In this work, a two-step hierarchical micromechanics approach has been presented for the modeling of particle-reinforced unsaturated porous composites with interface effects that find applications in the field of smart multi-functional structural materials. Firstly, particle-reinforced matrices are homogenized within a three-phase homogenization scheme (matrix/interphase/particle) by means of a double-inclusion method. Herein, both soft (overlapping) and hard (non-overlapping) interfaces are accounted for by finite interphases of constant thickness surrounding the particles. Furthermore, the presence of unsaturated pores is taken into account as equivalent homogeneous inclusions with elastic properties computed by the Reuss iso-stress approximation. Finally, the second step consists of the application of the Mori-Tanaka model to compute the macroscopic properties, considering the matrix/interphase/particle composites as homogeneous matrix phases and equivalent homogeneous pores as embedded ellipsoidal inclusions. Extensive numerical tests have been provided to demonstrate the effectiveness of the proposed micromechanics approach. First, both comparison against experimental data and sensitivity analyses have been presented for nano-sized particle-reinforced composites with hard interphases. Interestingly, a nonlinear regression fitting has been shown effective to determine the uncertain interphase parameters, including the interphase thickness and elastic modulus. Afterward, a similar scheme of results has been presented for the modeling of micro-sized particle-reinforced composites with soft interphases. Finally, numerical results have been also provided to give some insight into the constitutive relations of particle-reinforced unsaturated porous composites. Overall, the present approach is envisaged to provide a valuable numerical tool to quantitatively predict the macroscopic stiffness of particle-reinforced porous composites, including complex micromechanical features such as interface effects and unsaturated porosity, within a tractable and computationally inexpensive mathematical framework.

Acknowledgement

This work was supported by the Ministerio de Economía y Competitividad of Spain under the project DPI2014-53947-R. E. G-M was also supported by a FPU contract-fellowship from the Spanish Ministry of Education Ref: FPU13/04892. The financial support is gratefully acknowledged. The support of the Italian Ministry of Education, University and Research (MIUR) through the funded Project of Relevant National Interest SMART-BRICK: Novel strain-sensing nanocomposite clay brick enabling self-monitoring masonry structures (protocol no. 2015MS5L27) is also acknowledged.

References

[1] S. Bhogi, J. Nampoothiri, K. R. Ravi, M. Mukherjee, Influence of nano and micro particles on the expansion and mechanical properties of aluminum foams, Materials Science and Engineering: A 685 (2017) 131–138.

[2] H. M. Irshad, B. A. Ahmed, M. A. Ehsan, T. I. Khan, T. Laoui, M. R. Yousaf, A. Ibrahim, A. S. Hakeem, Investigation of the structural and mechanical properties of micro-/nano-sized Al_2O_3 and cBN composites prepared by spark plasma sintering, Ceramics International 43 (2017) 10645–10653.

[3] A. Downey, A. D'Alessandro, S. Laflamme, F. Ubertini, Smart bricks for strain sensing and crack detection in masonry structures, Smart Materials and Structures 27 (2017) 015009.

[4] J. A. Casado, F. Gutiérrez-Solana, I. Carrascal, S. Diego, J. A. Polanco, D. Hernández, Fatigue behavior enhancement of short fiber glass reinforced polyamide by adding phase change materials, Composites Part B: Engineering 93 (2016) 115–122.

[5] F. Deng, Y. Guan, Z. Shi, F. Wang, X. Che, Y. Liu, Y. Wang, The effect of dopamine modified titanium dioxide nanoparticles on the performance of poly (vinyl alcohol)/titanium dioxide composites, Composites Science and Technology 150 (2017) 120–127.

[6] A. H. Korayem, N. Tourani, M. Zakertabrizi, A. M. Sabziparvar, W. H. Duan, A review of dispersion of nanoparticles in cementitious matrices: Nanoparticle geometry perspective, Construction and Building Materials 153 (2017) 346–357.

[7] Y. Gowayed, J. Pierce, D. Buchanan, L. Zawada, R. John, K. Davidson, Effect of microstructural features and properties of constituents on the thermo-elastic properties of ceramic matrix composites, Composites Part B: Engineering 135 (2018) 155–165.

[8] F. Ubertini, A. D'Alessandro, A. L. Materazzi, S. Laflamme, A. Downey, Novel nanocomposite clay brick for strain sensing in structural masonry, IEEE, 2017, pp. 1–4.

[9] Y. Han, Y. Yang, L. Wang, X. Chen, Z. H. Chu, X. N. Zhang, Y. C. Dong, Z. Liu, D. R. Yan, J. X. Zhang, C. G. Li, Microstructure and properties of in-situ TiB_2 matrix composite coatings prepared by plasma spraying, Applied Surface Science 431 (2018) 48–54.

[10] J. K. Nelson, J. C. Fothergill, L. A. Dissado, W. Peasgood, Towards an understanding of nanometric dielectrics, in: Electrical Insulation and Dielectric Phenomena, 2002 Annual Report Conference on, IEEE, 2002, pp. 295–298.

[11] X. Cheng, K. W. Putz, C. D. Wood, L. C. Brinson, Characterization of local elastic modulus in confined polymer films via AFM indentation, Macromolecular rapid communications 36 (2015) 391–397.

[12] F. R. Jones, Interphase formation and control in fibre composite materials, volume 116, Trans Tech Publ, 1996, pp. 41–60.

[13] A. K. M. Masud, N. Tahreen, F. Abedin, Effects of interphase and matrix properties on effective tensile elastic modulus of carbon nanotube-based composite, Journal of Mechanical Engineering 40 (2009) 29–38.

[14] F. T. Fisher, L. C. Brinson, Viscoelastic interphases in polymer-matrix composites: theoretical models and finite-element analysis, Composites Science and technology 61 (2001) 731–748.

[15] J. M. Torralba, F. Velasco, C. E. Costa, I. Vergara, D. Cáceres, Mechanical behaviour of the interphase between matrix and reinforcement of Al 2014 matrix composites reinforced with $(Ni_3AL)_p$, Composites Part A: Applied Science and Manufacturing 33 (2002) 427–434.

[16] F. Lebon, S. Dumont, R. Rizzoni, J. López-Realpozo, R. Guinovart-Díaz, R. Rodríguez-Ramos, J. Bravo-Castillero, F. J. Sabina, Soft and hard anisotropic interface in composite materials, Composites Part B: Engineering 90 (2016) 58–68.

[17] W. Xu, F. Wu, Y. Jiao, M. Liu, A general micromechanical framework of effective moduli for the design of nonspherical nano-and micro-particle reinforced composites with interface properties, Materials & Design 127 (2017) 162–172.

[18] Y. W. Chang, S. Kim, Y. Kyung, Poly (butylene terephthalate)-clay nanocomposites prepared by melt intercalation: morphology and thermomechanical properties, Polymer International 54 (2005) 348–353.

[19] Y. Zare, K. Y. Rhee, Multistep modeling of Young's modulus in polymer/clay nanocomposites assuming the intercalation/exfoliation of clay layers and the interphase between polymer matrix and nanoparticles, Composites Part A: Applied Science and Manufacturing 102 (2017) 137–144.

[20] J. P. Ollivier, J. C. Maso, B. Bourdette, Interfacial transition zone in concrete, Advanced Cement Based Materials 2 (1995) 30–38.

[21] Y. Gao, G. De Schutter, G. Ye, Z. Tan, K. Wu, The ITZ microstructure, thickness and porosity in blended cementitious composite: Effects of curing age, water to binder ratio and aggregate content, Composites Part B: Engineering 60 (2014) 1–13.

[22] Z. Hashin, Composite materials with interphase: Thermoelastic and inelastic effects, Springer, 1991, pp. 3–34.

[23] Y. Benveniste, T. Miloh, Imperfect soft and stiff interfaces in two-dimensional elasticity, Mechanics of materials 33 (2001) 309–323.

[24] M. P. Lutz, R. W. Zimmerman, Effect of an inhomogeneous interphase zone on the bulk modulus and conductivity of a particulate composite, International Journal of Solids and Structures 42 (2005) 429–437.

[25] M. Rouhi, M. Rais-Rohani, Modeling and probabilistic design optimization of a nanofiber-enhanced composite cylinder for buckling, Composite Structures 95 (2013) 346–353.

[26] C. C. Yang, Effect of the transition zone on the elastic moduli of mortar, Cement and Concrete Research 28 (1998) 727–736.

[27] F. Deng, K. J. Van Vliet, Prediction of elastic properties for polymer-particle nanocomposites exhibiting an interphase, Nanotechnology 22 (2011) 165703.

[28] R. M. Christensen, K. H. Lo, Solutions for effective shear properties in three phase sphere and cylinder models, Journal of the Mechanics and Physics of Solids 27 (1979) 315–330.

[29] X. L. Ji, J. K. Jing, W. Jiang, B. Z. Jiang, Tensile modulus of polymer nanocomposites, Polymer Engineering & Science 42 (2002) 983–993.

[30] A. S. Sarvestani, On the overall elastic moduli of composites with spherical coated fillers, International journal of solids and structures 40 (2003) 7553–7566.

[31] M. Majewski, M. Kursa, P. Holobut, K. Kowalczyk-Gajewska, Micromechanical and numerical analysis of packing and size effects in elastic particulate composites, Composites Part B: Engineering 124 (2017) 158–174.

[32] E. Herve, A. Zaoui, N-layered inclusion-based micromechanical modelling, International Journal of Engineering Science 31 (1993) 1–10.

[33] Y. M. Wu, Z. P. Huang, Y. Zhong, J. Wang, Effective moduli of particle-filled composite with inhomogeneous interphase: Part I-bounds, Composites science and technology 64 (2004) 1345–1351.

[34] G. Pal, S. Kumar, Multiscale modeling of effective electrical conductivity of short carbon fiber-carbon nanotube-polymer matrix hybrid composites, Materials & Design 89 (2016) 129–136.

[35] M. Wang, N. Pan, Predictions of effective physical properties of complex multiphase materials, Materials Science and Engineering: R: Reports 63 (2008) 1–30.

[36] C. Shi, Q. Tu, H. Fan, C. A. O. Rios, S. Li, Interphase models for nanoparticle-polymer composites, Journal of Nanomechanics and Micromechanics 6 (2016) 04016003.

[37] J. J. Beaudoin, R. F. Feldman, P. J. Tumidajski, Pore structure of hardened Portland cement pastes and its influence on properties, Advanced Cement Based Materials 1 (1994) 224–236.

[38] R. W. Zimmerman, M. S. King, P. J. M. Monteiro, The elastic moduli of mortar as a porous-granular material, Cement and Concrete Research 16 (1986) 239–245.

[39] Y. Guéguen, T. Chelidze, M. Le Ravalec, Microstructures, percolation thresholds, and rock physical properties, Tectonophysics 279 (1997) 23–35.

[40] K. Miled, K. Sab, R. Le Roy, Effective elastic properties of porous materials: Homogenization schemes vs experimental data, Mechanics Research Communications 38 (2011) 131–135.

[41] L. Poh, C. Della, S. Ying, C. Goh, Y. Li, Micromechanics model for predicting effective elastic moduli of porous ceramic matrices with randomly oriented carbon nanotube reinforcements, AIP Advances 5 (2015) 097153.

[42] A. Rahmouni, A. Boulanouar, A. Samaouali, M. Boukalouch, Y. Graud, J. Sebbani, Prediction of elastic and acoustic behaviors of calcarenite used for construction of historical monuments of Rabat, Morocco, Journal of Rock Mechanics and Geotechnical Engineering 9 (2017) 74–83.

[43] W. Xu, H. Ma, S. Ji, H. Chen, Analytical effective elastic properties of particulate composites with soft interfaces around anisotropic particles, Composites Science and Technology 129 (2016) 10–18.

[44] M. Hori, S. Nemat-Nasser, Double-inclusion model and overall moduli of multi-phase composites, Mechanics of Materials 14 (1993) 189–206.

[45] S. Nemat-Nasser, M. Hori, Micromechanics: overall properties of heterogeneous materials, volume 37, Elsevier, 2013.

[46] S. C. Lin, T. Mura, Elastic fields of inclusions in anisotropic media (II), Physica Status Solidi (a) 15 (1973) 281–285.

[47] T. Mura, Micromechanics of defects in solids, volume 3, Springer Science & Business Media, 1987.

[48] T. W. Chou, S. Nomura, M. Taya, A self-consistent approach to the elastic stiffness of short-fiber composites, Journal of Composite Materials 14 (1980) 178–188.

[49] J. K. Beddow, Particle Characterization in Technology: Volume II: Morphological Analysis, CRC press, 2018.

[50] S. N. Domenico, Effect of brine-gas mixture on velocity in an unconsolidated sand reservoir, Geophysics 41 (1976) 882–894.

[51] P. Carballeira, F. Haupert, Toughening effects of titanium dioxide nanoparticles on TiO_2/epoxy resin nanocomposites, Polymer composites 31 (2010) 1241–1246.

[52] I. O. Yaman, N. Hearn, H. M. Aktan, Active and non-active porosity in concrete part I: experimental evidence, Materials and Structures 35 (2002) 102.